metals

MDPI

Article

Structure and Properties of Stainless Steel–Thermoplastic Joints Made Using Resistance Element Soldering Technology

Pavol Sejč [1,*], Pavol Švec [1], Peter Gogola [2], Branislav Vanko [1], Zuzana Gábrišová [1], Alexander Schrek [1] and Miroslav Zelina [3]

[1] Institute of Technologies and Materials, Faculty of Mechanical Engineering, Slovak University of Technology in Bratislava, Námestie slobody 17, 812 31 Bratislava, Slovakia; branislav.vanko@stuba.sk (B.V.); zuzana.gabrisova@stuba.sk (Z.G.); alexander.schrek@stuba.sk (A.S.)
[2] Institute of Materials Science, Faculty of Materials Science and Technology in Trnava, ul. Jána Bottu 25, 917 24 Trnava, Slovakia; peter.gogola@stuba.sk
[3] Institute of Materials and Machine Mechanics, Slovak Academy of Sciences, Dúbravská cesta 9, 845 13 Bratislava, Slovakia; miroslav.zelina@savba.sk
* Correspondence: pavol.sejc@stuba.sk; Tel.: +421-905-326-211

Abstract

This study investigated the microstructure and properties of soldered joints of AISI 304 stainless steel and PMMA thermoplastic or AW-1050A aluminum alloys made using Resistance Element Soldering (RES) technology. The bimetallic element used in RES provided a mechanical joint with a thermoplastic or aluminum alloy and a soldered joint with AISI 304 steel using Sn60Pb40 solder in the core of the element. The solder in combination with the Chemet CHM-A-014 flux wetted the AISI 304 steel surface very well at a temperature of 225 °C with a contact angle of 14°. During the production of the joints, the solder melted in the bimetallic element on the AISI 304 steel side, while solid solder was retained at the point of contact with the welding electrode. The strength of the joints ranged from 25.5 to 36.4 MPa, which was less than the strength of the solder, and the joints failed at the AISI 304 steel–Sn60Pb40 solder interface. The fracture surface was predominantly formed by the solder. An intermetallic phase of $FeSn_2$ was identified at the interface.

Keywords: metal-to-plastic joining; soldering; resistance heating

1. Introduction

Research into soldering of high-alloy steels is currently focused mainly on the possibilities of joining steel to non-metallic materials [1,2] by using different energy sources [2–4] and research into the properties of soldered joints [5]. Among new joining technologies, we can also include Resistance Element Soldering (RES) technology, which is fundamentally based on Resistance Element Welding (REW) technology and is described in detail in the papers [6–8]. RES technology was designed for joining metals to thermoplastics by resistance heating. The essential difference between RES and REW is that instead of a base element, a bimetallic element is used (Figure 1), where the housing ensures a mechanical connection to the thermoplastic and the solder core ensures a metallurgical joint to the metal. The relatively low melting temperature of the Sn-based solder (depending on the composition around 200 °C) enables resistance soldering without the risk of thermal degradation of the plastic.

Heat generation during resistance heating at the interface of the materials to be joined [9], precise heat dosing, and the significantly different melting temperatures of

Check for updates

Academic Editor: Antonio Riveiro

Received: 21 November 2025
Revised: 15 December 2025
Accepted: 17 December 2025
Published: 20 December 2025

Copyright: © 2025 by the authors. Licensee MDPI, Basel, Switzerland. This article is an open access article distributed under the terms and conditions of the Creative Commons Attribution (CC BY) license.

Sn solders and steels affect the volume of molten solder. With appropriately selected resistance heating parameters in RES technology (Figure 1), the soldering temperature is reached at the solder–steel interface. At the solder–electrode interface, the temperature does not exceed the melting temperature of the solder due to intensive heat removal through the water-cooled electrode [10]. Such a temperature distribution is advantageous in terms of minimizing the wear of the contact surfaces of the electrodes, which occurs, for example, in resistance welding of galvanized steel sheets [11–13].

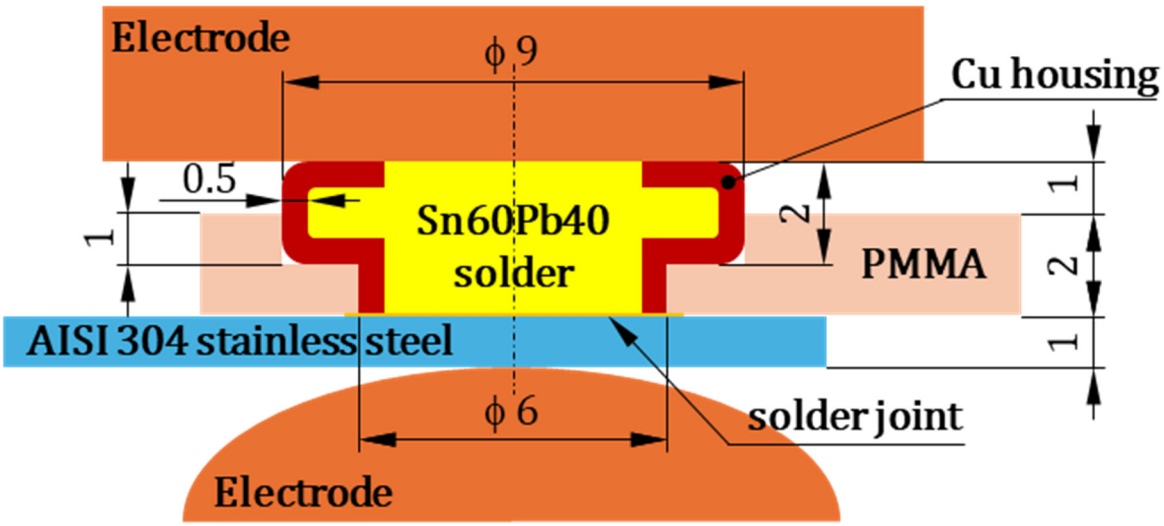


Figure 1. Joint produced by RES using a bimetallic element.

The results published in the paper [8] indicate the possible potential of RES technology in joining galvanized steel sheets to PMMA using Sn60Pb40 solder. Sn-Pb solders have been the most widely used material for soldering of Cu- and Fe-based metallic materials for decades [14,15]. In addition to good wettability and strength, they also exhibit high resistance to brittle failure at cryogenic temperatures [16]. Possible alternatives for soldering high-alloy steels are lead-free solders of the Sn91Zn9 and Sn96Sb4 types [5]. When verifying the suitability of using modified Sn solders, the results achieved (e.g., mechanical properties of joints) are usually verified by comparing them with the properties of joints made with Sn-Pb solders [17].

The soldering of stainless steels is significantly influenced by the properties of the passivation layer that forms on the surface of the material when exposed to the air atmosphere. Despite the ambiguity in the composition of the layer, research teams agree that the passivation coating consists of two layers of oxides and hydroxides of iron and chromium [18]. Passivation occurs by the rapid formation of surface-adsorbed hydrated metal complexes that are sufficiently stable on the alloy surface so that further reaction with water allows the formation of a hydroxide phase that forms an insoluble, surface oxide film [19].

Chromium is the main element in the passivation layer. At chromium contents above 10.5 to 11.5%, steel can form a protective coating with a thickness of several nanometers. The protective coating is enriched with iron in addition to chromium, but the structure of passivated films on stainless steels is determined by chromium [20,21]. The three most commonly used austenite stabilizers—nickel, manganese and nitrogen—contribute to the passivation of the surface of austenitic stainless steels [22]. Nickel is generally not found inside the passivation layer, but the interface below this layer is enriched with nickel. Analysis of the layer of metal samples exposed to the air atmosphere showed the presence of carbon and oxygen. Carbon is present mainly due to adsorbed hydrocarbons. Oxygen

comes from the immediate formation of oxides as well as from adsorbed water vapor and carbon dioxide. A clean metal surface is very reactive and adsorbs more water vapor and atmospheric contaminants than a contaminated surface [23].

Stainless steel is not an easy material to solder for two reasons. First, it is covered with an extremely stable passivation layer. Second, stainless steel has a relatively low thermal conductivity, which makes it difficult to heat the joints quickly and evenly to the soldering temperature [14,24]. To ensure the wettability and flowability of the liquid solder, the surface of the base material must be cleaned before soldering. Cleaning requires a two-step process: removal of oil and grease, followed by removal of oxides. Suitable methods include steam degreasing, solvent degreasing, acid pickling, blasting, and grinding with a wire brush or stainless steel abrasive cloth. If the surfaces are highly polished, it is best to roughen them slightly with an abrasive cloth or other suitable means before soldering. Soldering should be carried out immediately after cleaning. If soldering is delayed, the parts to be joined should be pre-coated with solder immediately after cleaning [24].

When soldering steels, it is necessary to apply a flux to remove surface oxides, thereby creating suitable conditions for the wettability and flowability of the molten solder. In the case of corrosion-resistant steels, the surface oxides are rich in chromium. This gives stainless steels corrosion resistance but is more difficult to remove than oxides formed on unalloyed carbon steels. In soldering, fluxes based on orthophosphoric acid and hydrochloric acid, as well as aqueous solutions of zinc chloride, are suitable due to the properties of the passivation layer. If the alloy being soldered contains molybdenum, titanium, niobium or aluminum, the flux should also contain a certain amount of hydrofluoric acid [24].

Commercially available solders, mostly based on Sn, can be used for soldering of stainless steels, which have been used mainly in electrical engineering [25]. In general, the higher the tin content of the solder, the better the wetting and flow on stainless steel [24]. Eutectic or nearly eutectic Sn-Pb solders have traditionally been a favored choice by electronics manufacturers because of their exceptional soldering capabilities and reliability [25]. The composition of stainless steel suggests that the solder should promote metallurgical reactions with the main elements of this steel, namely Fe and Ni, in order to promote surface wetting. Tin-based solders wet Fe and Ni well. However, the phase diagram of the binary Cr-Sn alloy shows almost complete mutual insolubility of Cr and Sn in the solid phase [26]. High-Sn alloys are preferred for use on stainless steels, not only because of the maximization of the metallurgical reaction at the solder/base interface and low melting temperatures, but also due to their good strength, thus meeting many of the service conditions for which stainless steels are selected [24].

Current knowledge shows the potential of RES technology in joining galvanized non-alloy steel sheets to plastics, while alloyed steels have not been the subject of research so far. For this reason, our study was focused on evaluating the influence of RES parameters on the microstructure and some properties of AISI 304 stainless steel soldered to thermoplastic joints.

2. Experiment

2.1. Materials and Joint Geometry

In the study of the influence of RES parameters on the properties of the joints, austenitic stainless steel AISI 304 was joined to a thermoplastic of PMMA type or an aluminum alloy AW-1050A using a bimetallic element. The geometry of the assembly for RES is shown in Figures 1 and 2. Blanks with dimensions of 30 × 100 × 1 mm were prepared by cutting them from cold-rolled AISI 304 sheets with a thickness of 1 mm. The sheet metal used had one side polished and the other ground. The soldered joint was made on the ground side of the sheet, which had an average roughness Ra of 0.25 µm. The rough side was selected due

to the assumed better wetting conditions compared to the polished side [24]. The chemical composition and mechanical properties of AISI 304 steel are given in Tables 1 and 2 [27]. Steel is characterized by a relatively low thermal conductivity of 16.2 $W.m^{-1}.K^{-1}$ [23]. For the production of test samples, thermoplastic blanks with dimensions of 30 × 100 × 2 mm were cut from a PMMA sheet, with the trade name QUINN XT. This plastic was chosen because of its transparency, which enabled visual inspection of the soldering point. Selected properties of the PMMA QUINN XT are given in Table 3 [28]. A ∅ 6 hole with a ∅ 9 × 1 recess was drilled in the PMMA to properly position the element and allow for its axial deformation during joining. The dimensions of the used blanks of the overlapped joints were based on the dimensions of test samples used in works with a similar focus, e.g., [29].

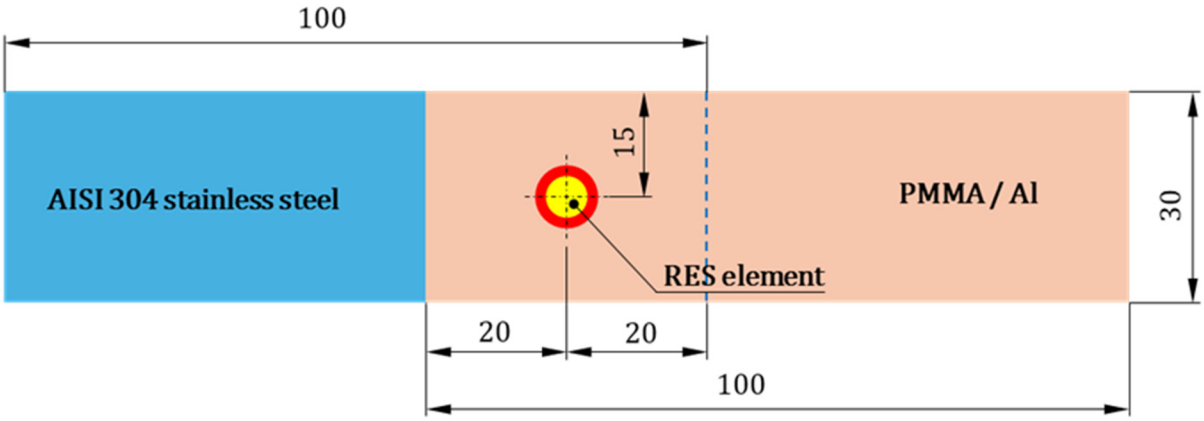


Figure 2. Geometry of the assembly for RES.

Table 1. Chemical composition of AISI 304 stainless steel.

Element	C	Mn	Si	P	S	Cr	Ni	N
wt. %	<0.08	<2.0	<0.75	<0.045	<0.03	18 ÷ 20	8.0 ÷ 10.5	<0.1

Table 2. Mechanical properties of AISI 304 stainless steel.

Yield Strength R_e (MPa)	Ultimate Tensile Strength R_m (MPa)	Elongation at Break A (%)
>205	>515	>40

Table 3. Mechanical and thermal properties of PMMA QUINN XT thermoplastic.

Ultimate Tensile Strength R_m (MPa)	Elongation at Break A (%)	Max. Working Temperature T_W (°C)	Degradation Temperature T_D (°C)	Molding Temperature T_M (°C)
>70	>4	85	>280	130 ÷ 170

When designing the dimensions of bimetallic elements, we based our work on the dimensions of the elements used in REW technology. This technology uses elements with a shank diameter of 5 or 6 mm [30–34], and the diameter and height of the head depend on the type and thickness of the material on which the form-fit connection is applied. We chose a shank diameter of 6 mm for RES technology, since, in general, a larger contact area of the soldered joint has a positive effect on its load-bearing capacity.

In the joints intended for measuring the mechanical properties, the PMMA blanks were replaced by AW-1050A blanks with identical dimensions except for the thickness, which was 1 mm. The chosen aluminum alloy had a higher strength than plastic, which

allowed us to test the strength of the soldered joint. When using plastic in the joint assembly, it broke under load in a place that was weakened by the pre-drilled hole. However, the plastic enabled visual inspection of the soldered joint. The composition and properties of the AW-1050A aluminum alloy used are given in Tables 4 and 5 [35].

Table 4. Chemical composition of AW-1050A aluminum alloy.

Element	Al	Si	Fe	Cu	Mn	Mg	Zn	Ti
wt. %	>99.5	<0.25	<0.40	<0.05	<0.01	<0.05	<0.07	<0.05

Table 5. Mechanical properties of AW-1050A aluminum alloy.

Yield Strength $R_{p0.2}$ (MPa)	Ultimate Tensile Strength R_m (MPa)	Elongation at Break A (%)
>85	105–145	>2

The bimetallic element (Figure 1) consisted of a housing formed by a Cu tube and a core filled with solder Sn60Pb40. The Cu tube had an outer diameter of Ø 6 mm and a wall thickness of 0.5 mm. The element was prepared by centrifugal casting of Sn60Pb40 solder into a Cu tube, subsequent cutting of bimetallic segments with a length of 11 mm, and cold extrusion of these segments. The production of the elements is described in detail in [36]. The mechanical properties, melting temperature, and electrical resistance of the materials of the bimetallic element are given in Table 6 [37,38].

Table 6. Properties of element materials.

Material	Ultimate Tensile Strength R_m (Mpa)	Ultimate Shear Strength τ_u (MPa)	Elongation at Break A (%)	Melting Point T_m (°C)	Electrical Resistance R (Ω)
Cu tube	>210	-	>60	1083	1.7×10^{-6}
Sn60Pb40	>56	>39	>60	183–190	1.5×10^{-5}

On the soldered interface of the RES joint (AISI 304 steel–Sn60Pb40 solder), a liquid flux Chemet CHM-A-014 was applied. This flux was specially designed for soldering stainless steel. The chemical composition of the flux is given in Table 7 [39].

Table 7. Chemical composition of Chemet CHM-A-014 flux.

Component	Content (wt.%)	Purpose
H_2O	55–70	Solvent
$ZnCl_2$	25–30	Activator, oxide remover
Propan-2-ol C_3H_8O	1–5	Solvent, wetting agent
NH_4Cl	1–5	Activator, complexation
HCL	1–5	Acid, activity enhancer

2.2. Wetting Measurement

To verify the selection of solder and flux for soldering of AISI 304 stainless steel, the wetting of Sn60Pb40 solder on the surface of AISI 304 steel was evaluated. Pieces of an AISI 304 steel sheet with dimensions of 38 × 38 × 1 mm were prepared for the test. These were cleaned with acetone in an ultrasonic cleaner for 3 min. After cleaning, a solder weighing 0.05 g was placed on the ground side of the sheet metal and a layer of flux was applied with

a brush. The prepared sample was heated in a chamber furnace. Wetting was quantitatively evaluated by the contact angle α. This was measured using an Axiovert 40 MAT light microscope (Carl Zeiss AG, Oberkochen, Germany) on a metallographic section prepared by a standard procedure.

2.3. Production and Evaluation of RES Joints

On steel blanks intended for the production of RES joints, a layer of solder was pre-applied to the surfaces (about half of the blank). Before applying it, each blank was cleaned with acetone in an ultrasonic cleaner for 3 min. Subsequently, flux was applied with a brush, and the specified part of the blank was immersed in molten solder with a temperature of 225 °C for 10 s. After the sample was pulled out, a layer of solder was formed on the immersed surface with free cooling in air. The average thickness of the applied solder layer was 0.03 mm. The purpose of creating the layer of solder was to ensure suitable conditions for the formation of a soldered joint between the element and the stainless steel during resistance heating. The short resistance heating time (usually within 1 s) [40] and the low thermal conductivity of stainless steel (16.2 $W.m^{-1}.K^{-1}$) represent a fundamental problem in heating the flux, solder, and base material to the soldering temperature over the entire contact area [41].

After re-cleaning the joined segments (steel blank with a layer of solder, thermoplastic and bimetallic element) with acetone in an ultrasonic cleaner for 3 min, the individual parts of the assembly were arranged according to Figure 2. For resistance heating of the bimetallic element during joining, an ARO XMA 36kVA welding gun (ARO S.A.S., Château-du-Loir, France) with a VTS control system of the ULB 1.4 type (VTS Electro s.r.o., Bratislava, Slovakia) was used. The universal control system allowed us to set the resistance heating time and power source from 20 to 99%. For this reason, it was necessary to use a Miyachi–Weld Checker MM-356 B measuring device (Miyachi Technos Corporation, Arakawaku, Tokyo, Japan) to determine the welding current and voltage.

Based on initial experiments, the power source was set to 20%, the heating time to 0.5 s, and the clamping force to 800 N when manufacturing all tested samples. The measured parameters during the production of RES joints are given in Table 8, from which it can be seen that the applied electric voltage and current differed slightly. These differences were probably caused by slightly different resistance heating conditions at the bimetallic element–AISI 304 steel interface, which are influenced by the properties of the contact surfaces. Based on these parameters, the heat input of the soldering (Q) was calculated according to Equation (1):

$$Q = I.U.t \text{ (J)}, \quad (1)$$

where

U is voltage (V);
I is electric current (A);
t is heating (soldering) time (s).

Table 8. Resistance heating parameters for the production of test samples.

Joining Parameter	Sample number						
	PMMA1	PMMA2	Al1	Al2	Al3	Al4	Al5
U (V)	0.59	0.59	0.58	0.56	0.55	0.52	0.59
I (kA)	3.24	3.28	3.23	3.35	3.28	3.34	3.25
Q (J)	956	968	937	938	902	868	959

The prepared RES joint samples were subjected to visual inspection. For this purpose, samples with thermoplastic were used. The microstructure of the joints on cross-sections prepared by a standard metallographic procedure was evaluated on selected samples. Light microscopy using the Axiovert 40 MAT microscope (Carl Zeiss AG, Oberkochen, Germany) and scanning electron microscopy (SEM) using a JEOL JSM-IT300 electron microscope (JEOL Ltd., Akishima, Tokyo, Japan) were used to observe the microstructure. The local chemical composition was measured using the Oxford Instruments X-Max 20 EDS spectrometer (Oxford Instruments NanoAnalysis & Asylum Research, High Wycombe, UK), which is part of the electron microscope. To measure the strength of the joints, samples with an aluminum alloy were used. The samples were tested for tensile strength on an Inspect Desk 5 testing machine (Hegewald & Peschke, Meß- und Prüftechnik GmbH Am Gründchen 1, 01683 Nossen, Germany)at a crosshead speed of 5 mm.min^{-1}. The morphology of the fracture surfaces after the tensile test was observed with a JEOL JSM-IT300 microscope. The phase composition was analyzed using X-ray diffraction (XRD) analysis. Measurements were performed using a PANalytical EMPYREAN diffractometer (Malvern Panalytical Ltd., Malvern, UK) system configured in a Bragg–Brentano geometry. The system was equipped with a PIXcel3D detector operating in 1D scanning mode. A cobalt (Co) anode X-ray tube was used as the radiation source, operating at 40 kV and 40 mA. Measurements were conducted in continuous scan mode across a 2Theta range of 20° to 130°. The phase quality was analyzed using the PANalytical Xpert High Score program (HighScore Plus version 3.0.5) with the ICSD FIZ Karlsruhe database.

3. Results and Discussion

3.1. Wetting the Surface of AISI 304 Stainless Steel with Sn60Pb40 Solder

The evaluation of the wettability of Sn60Pb40 solder on the surface of AISI 304 stainless steel is documented in Figure 3. The sample was heated in a chamber furnace at a temperature of 225 °C for 5 min.

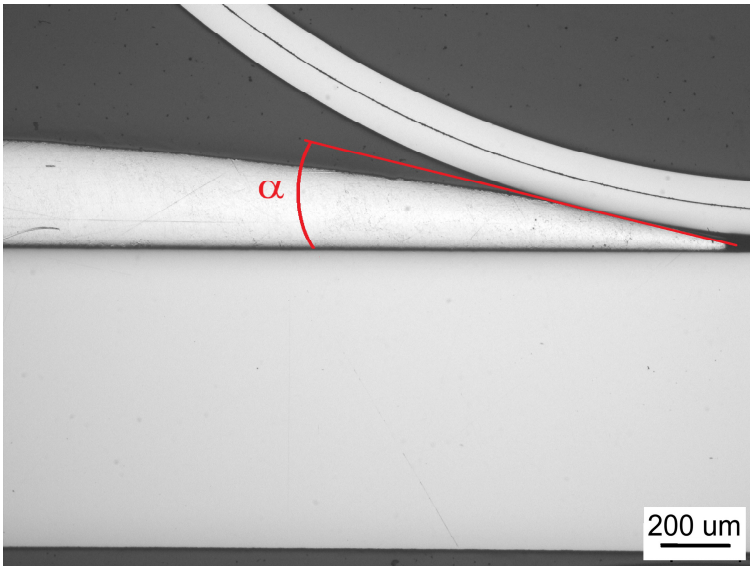


Figure 3. Wetting angle of AISI 304 with Sn60Pb40 solder.

The wetting angle of AISI 304 steel with Sn60Pb40 solder (α), measured on the solder cross-section, was 14°. The measurement result confirms the appropriate selection of solder and flux for the preparation of RES joints.

3.2. Visual Inspection of RES Joints

Table 8 provides an overview of the prepared joints, from which it is clear that two types of joints were prepared. The joints with the PMMA were intended for visual inspection and metallographic observation of the cross-sections of joints. The joints with the aluminum alloy were intended for strength tests and analysis of fracture surfaces. When visually evaluating the joints, no relevant differences were observed between the samples with the thermoplastic (PMMA1 and PMMA2). An overall view of the RES joint with the thermoplastic is documented in Figure 4a. Figure 4b shows the details of the joint area, which allowed solder spatter to be observed.

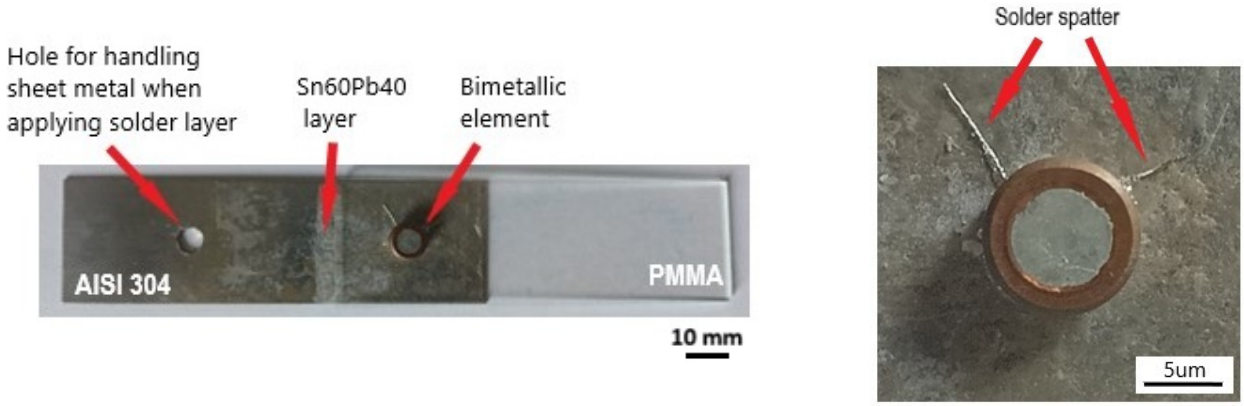


Figure 4. RES joint between AISI 304 steel and PMMA thermoplastic made using a bimetallic element: (**a**) general view, (**b**) joint details with solder spatter.

The overall view of the RES joint (Figure 4a) confirms the correct choice of resistance heating parameters in terms of the extent of deformation of the element, the volume of melted solder, and the thermal influence of the thermoplastic. Only rarely did solder spatter occur at the point of contact of the element with the steel sheet (Figure 4b). It can be assumed that the solder spatter during rapid heating, which is caused by pressure during the expansion of the melt volume, will be replaced at the joint point by molten solder from the core of the bimetallic element.

3.3. Structure of RES Joints

Figure 5 documents a cross-section of the RES joint. A certain volume of solder can be observed to melt in the core of the bimetallic element. The amount of melted solder during resistance heating of the element is directly related to the heat input used, as described in [4]. Isolated pores occurred in the core of the bimetallic elements (Figure 5). However, the porosity is localized outside the contact area between the element and the steel sheet. The porosity probably arose during the preparation of the semifinished bimetallic products by centrifugal casting [36].

Figure 6a documents the macrostructure of the RES joint section. Resistance heating allowed the desired temperature gradient to be achieved in the core of the bimetallic element with the maximum temperature reached at the point of contact with the AISI 304 sheet, as described in the Introduction. During soldering, extensive remelting of the solder in the core of the element occurred. The boundary between the melted and non-melted area is relatively clear and is related to the different grain size in the microstructure.

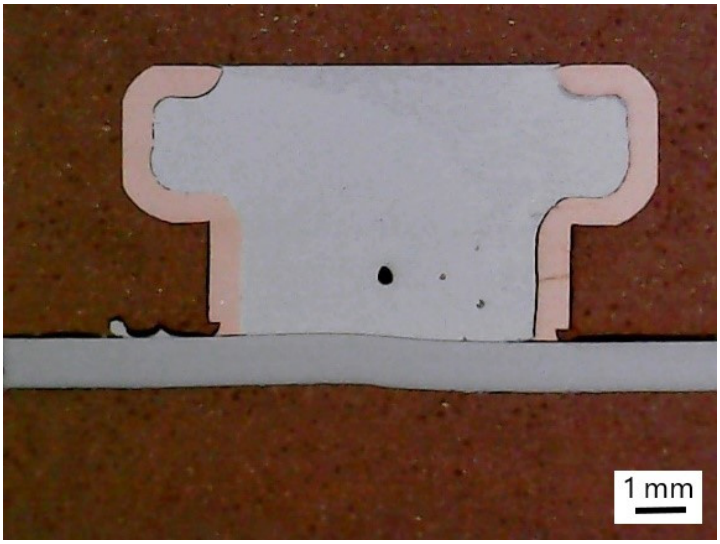


Figure 5. Cross-section of RES joint of AISI 304 steel and PMMA thermoplastic (PMMA1 sample).

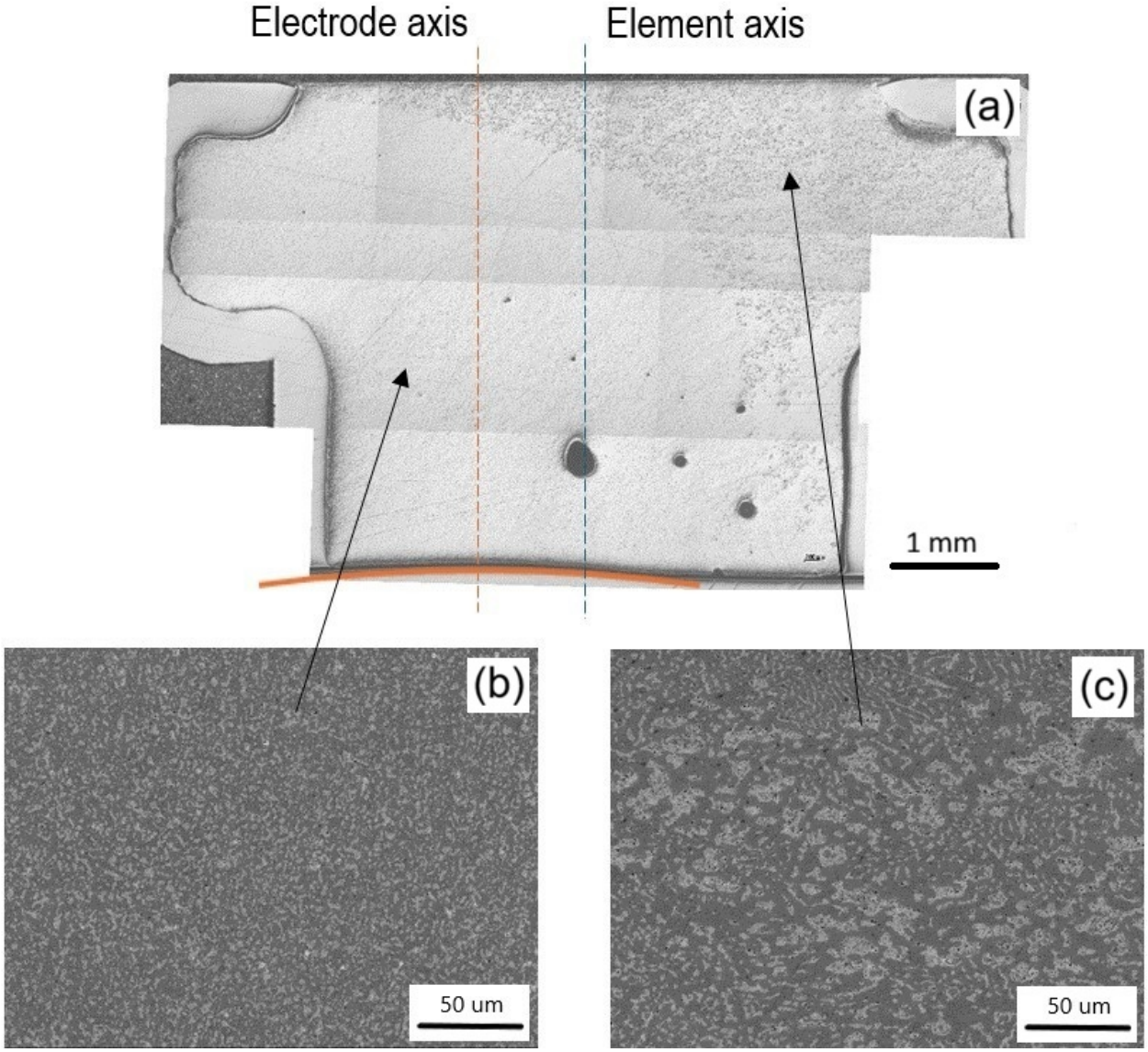
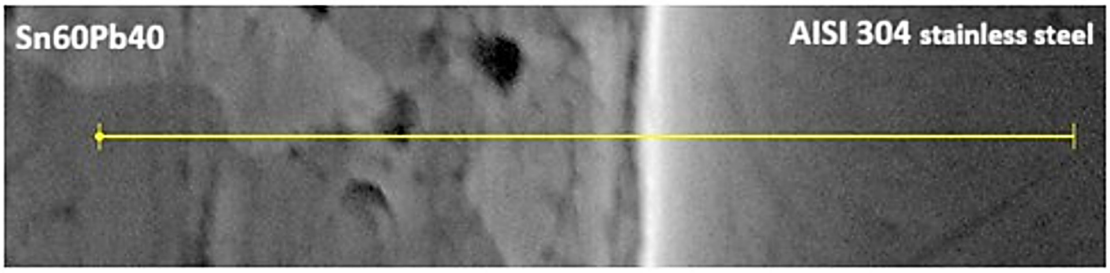


Figure 6. Structure of the element in the PMMA 1 sample: (**a**) macrostructure of the element, (**b**) fine-grained microstructure of the melted area, (**c**) coarse-grained microstructure of the non-melted area.

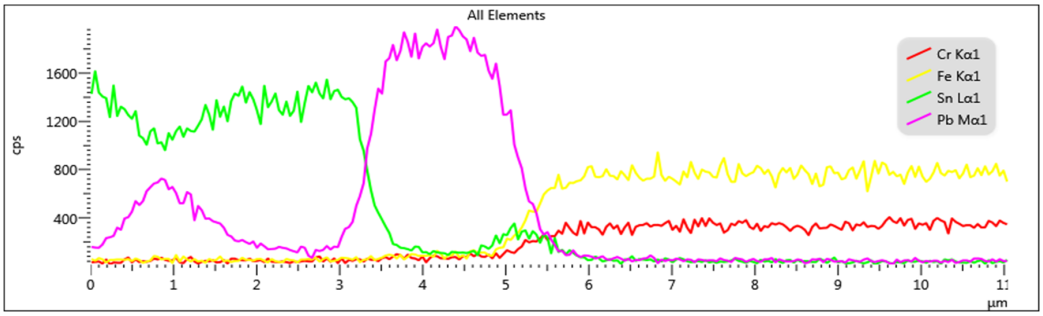
The microstructure of the solder with different grain sizes is documented in Figure 6b,c. Identical structural components were observed in both areas but with different dispersity. The microstructure of both areas was primarily formed by precipitated grains of a Pb-based solid solution and a eutectic mixture of Sn and Pb-based solid solutions. The observed microstructure corresponds to the equilibrium binary Sn–Pb diagram [41]. The short heating time and rapid cooling during resistance soldering caused the structural components in the remelted area to have a significantly smaller average grain size (below 5 μm) than in the non-melted area (above 15 μm). The asymmetric shape of the volume of remelted solder in the core of the element was caused by inaccuracy in the positioning of the electrodes of the welding gun.

Observation of the head of the element demonstrated solid-state contact at the electrode-element interface (upper edge in Figure 6a) during soldering. Solid-state contact confirmed the correct selection of heating parameters, which, with sufficiently intensive heat removal, ensured the correct temperature at the electrode–element interface. No solder melting occurred at this interface, which is favorable in terms of preserving the properties of the electrode. These could change as a result of enrichment of the Cu electrode with solder elements. The documented results of the application of a rapid temperature cycle (known from resistance spot welding) in soldering of high-alloy steels with Sn solders bring new insights that have not been investigated in more detail so far.

EDS line analysis of the distribution of elements across the soldered interface of the AISI 304 steel–Sn60Pb40 solder RES joint, which was measured in the center of the joint, is shown in Figure 7. In this image, a transition region can be observed on the solder side with a thickness of less than 1.5 μm. In this region, the wetted base material (AISI 304 steel) was dissolved by the molten solder. In this region, elements originating from both the steel (Cr, Fe) and the solder (Sn, Pb) were identified. The structural analysis of the transition region was supplemented by phase analysis on fracture surfaces.



(**a**)



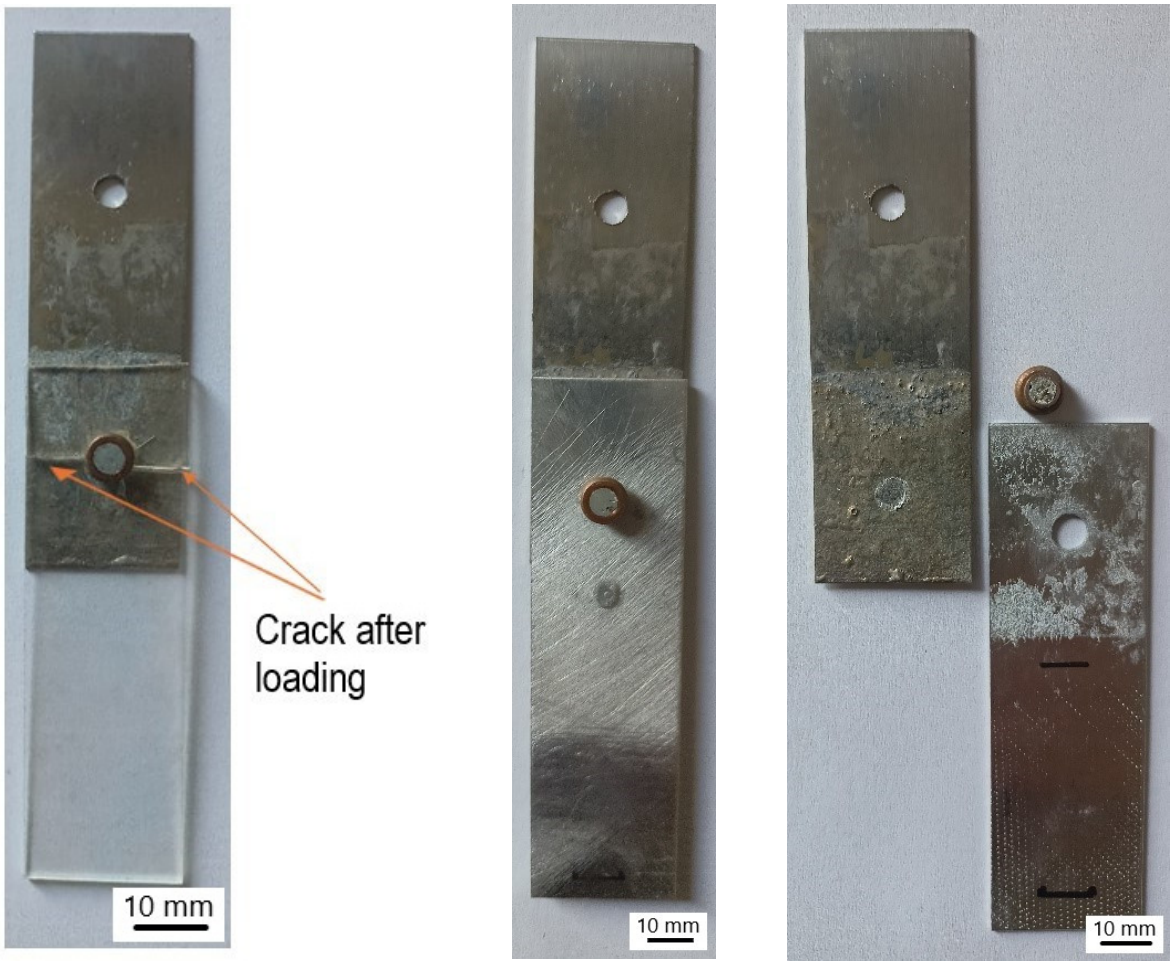
(**b**)

Figure 7. AISI 304 steel–Sn60Pb40 solder RES joint interface: (**a**) cross-section, (**b**) EDS line analysis of the distribution of elements across the interface.

3.4. Tensile Test of RES Joints

The test samples before and after the tensile test are documented in Figure 8. Figure 8a shows an overall view of the RES joint of the AISI 304 steel and PMMA thermoplastic after

the tensile test. The figure confirms that the overall strength of the joint exceeds the strength of the PMMA thermoplastic at the location weakened by the pre-drilled hole for the element. The strength of the connection between the PMMA and the Cu housing of the bimetallic element is determined only by the strength of the thermoplastic. When testing the PMMA1 and PMMA2 bonds (documented in Figure 8a), the strength expressed as F_{max} was at the level of 402 to 407 N. This fact justifies the replacement of the PMMA thermoplastic with the AW-1050A aluminum alloy (Figure 8b) for a quantified assessment of the strength of the soldered joint. The RES joint sample of the AISI 304 steel and AW-1050A aluminum alloy after the tensile test is shown in Figure 8c. This figure documents the failure of the joint at the AISI 304 steel–Sn60Pb40 solder interface. The tensile test results are given in Table 9. It can be seen from Figure 8 that the prepared lapped joints were subjected to shear force during strength testing. For this reason, it was possible to compare the strength of the soldered joints τ_m with the shear strength of the Sn60Pb40 solder τ_u (Table 6). It is clear from Table 9 that the strength of the joints ranged from 25.5 to 36.4 MPa, which represents 65 to 93% of the strength of the solder itself. The measured dispersion of the strength values could be caused by three factors: solder spattering and the formation of porosity; deviations in the heat input Q, which would also be conditioned by the possible misalignment of the element and the electrodes of the welding gun during heating; the surface conditions and force distribution on the contact surfaces between the element and the steel sheet.



(**a**) (**b**) (c)

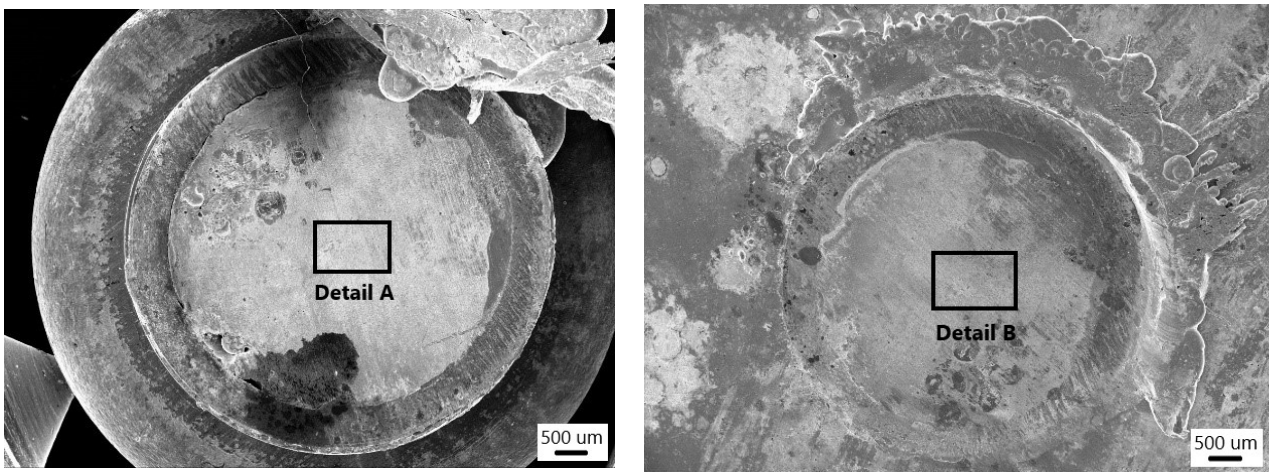
Figure 8. RES joints used for tensile test: (**a**) PMMA1 sample (AISI 304 steel–PMMA thermoplastic) after tensile test, (**b**) Al1 sample (AISI 304 steel–AW-1050A aluminum alloy) before tensile test, (**c**) Al1 sample after tensile test.

Table 9. Tensile test results.

Sample Parameter	Al1	Al2	Al3	Al4	Al5	Average Value
Shear force F_m (N)	808	1031	1010	721	914	897
Shear strength of the joint τ_m (MPa)	28.55	36.43	35.69	25.48	32.30	31.70
Shear strength ratio of the joint and the solder τ_m/τ_u	0.73	0.93	0.92	0.65	0.83	0.81

3.5. Analysis of Fracture Surfaces of RES Joints

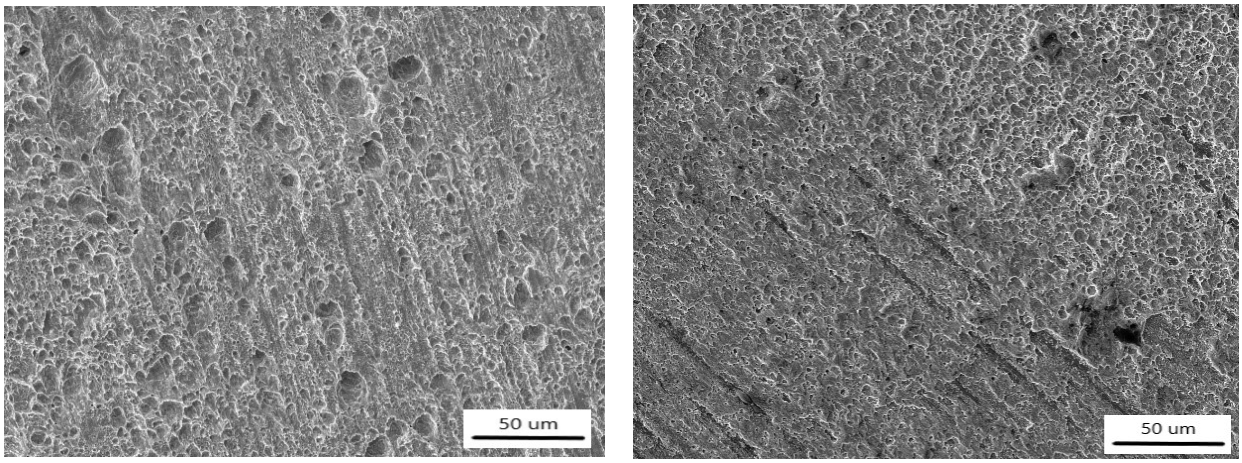
All tested joints failed at the soldered interface (AISI 304 steel–Sn60Pb40 solder). The fracture surfaces after the tensile test are documented in Figures 9 and 10. Figure 9a shows an overall view of the fracture surface of the soldered part of the joint from the element side. Figure 9b shows the fracture surface of the same joint from the AISI 304 sheet side. Observation of both fracture surfaces showed that the fracture of the joint occurred primarily through the solder material. Large areas with solder residues are evident on both fracture surfaces (Figure 9a,b). Figure 9b shows smaller areas where the surface of the steel sheet and solder spatter can be observed. Details of the dominant part of both fracture surfaces passing through the solder are documented in Figure 10a,b. Both figures show the pit morphology of the fracture surfaces of the Sn60Pb40 solder with a relatively regular shape and uniform distribution of pits. The morphology of the fracture surface indicates good toughness of the solder and failure by trans-grain ductile fracture. Such failure of Sn-based solders was observed at a temperature of 25 °C in another study [16]. The details of the fracture surface capturing the area of the Sn60Pb40 solder and the surface of the AISI 304 steel are shown in Figure 11a. EDS analysis of this surface is shown in Figure 11b, confirming the dominant presence of Sn and Pb from the solder. The small concentration of Fe and Cr corresponds to local failure of the joints on the steel surface (AISI 304 steel–Sn60Pb40 solder interface).



(**a**) (**b**)

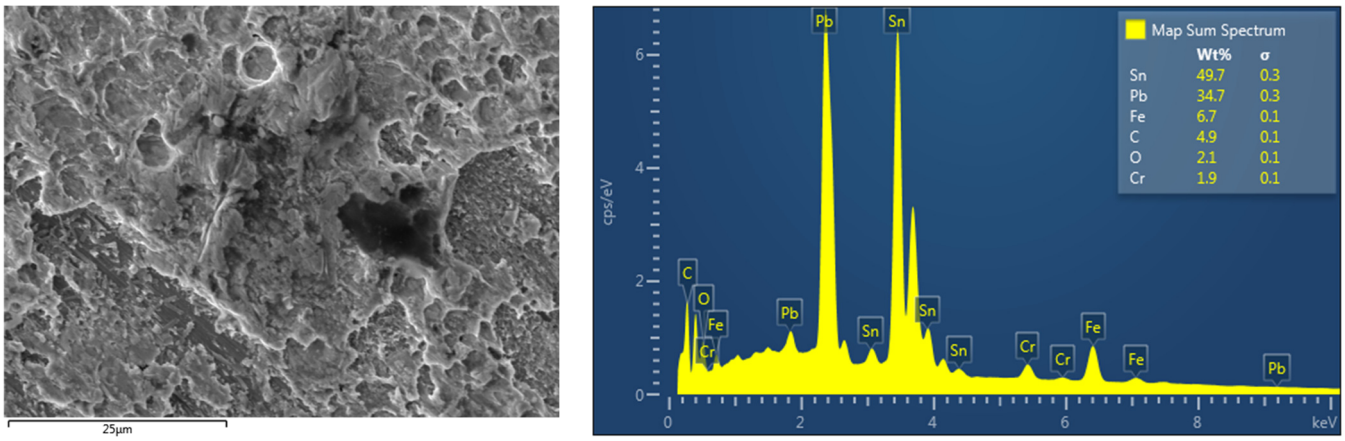
Figure 9. Overall view of the fracture surface from the side of the (**a**) element, (**b**) AISI 304 sheet.

The fracture surfaces of the joints were subjected to XRD phase analysis (Figure 12). Figure 12 documents the XRD records from the fracture surfaces of the three joints with the highest strength (Al2, Al3, Al5, see Table 9). For all three joints, the fracture surfaces on the AISI 304 steel side (Al2 sheet, Al3 sheet, Al5 sheet) and on the element side (Al2 element, Al3 element, Al5 element) were analyzed.



(**a**) (**b**)

Figure 10. Details of the fracture surface structure from the side of (**a**) element (Detail A), (**b**) AISI 304 sheet (Detail B).



(**a**) (**b**)

Figure 11. Analysis of the fracture surface of the joint from the side of the AISI 304 sheet: (**a**) fracture surface morphology, (**b**) EDS analysis.

XRD records in Figure 12 confirmed, in particular, the presence of structural components of the Sn60Pb40 solder on the analyzed fracture surfaces. In all records, Sn and Pb or their solid solutions are dominant, because the majority of the fracture surface passed through the solder. The records also showed the presence of Fe-gamma and Cu, the peaks of which overlap. The Fe-gamma peaks confirm that the fracture at the AISI 304 steel–solder interface and the Cu peaks come from the Cu housing of the element. The formation of a small amount of the intermetallic phase $FeSn_2$ on the fracture surfaces on the AISI 304 steel side (Al2 sheet, Al3 sheet, Al5 sheet) indicates the reaction of the solder with AISI 304 steel during soldering. The small proportion of the $FeSn_2$ phase is a consequence of a small part of the fracture surface being located outside the solder. Based on these records, it can be assumed that at the AISI 304 steel–Sn60Pb40 solder interface, an intermetallic phase $FeSn_2$ is formed during soldering. The small thickness of this phase did not enable its observation in the cross-section, but the formation of the transition region observed in Figure 7 confirms this assumption. The interface characteristics of soldered joints of high-alloy steels with Sn solders prepared through a rapid temperature cycle of resistance heating are valuable because they have not yet been described in the literature.

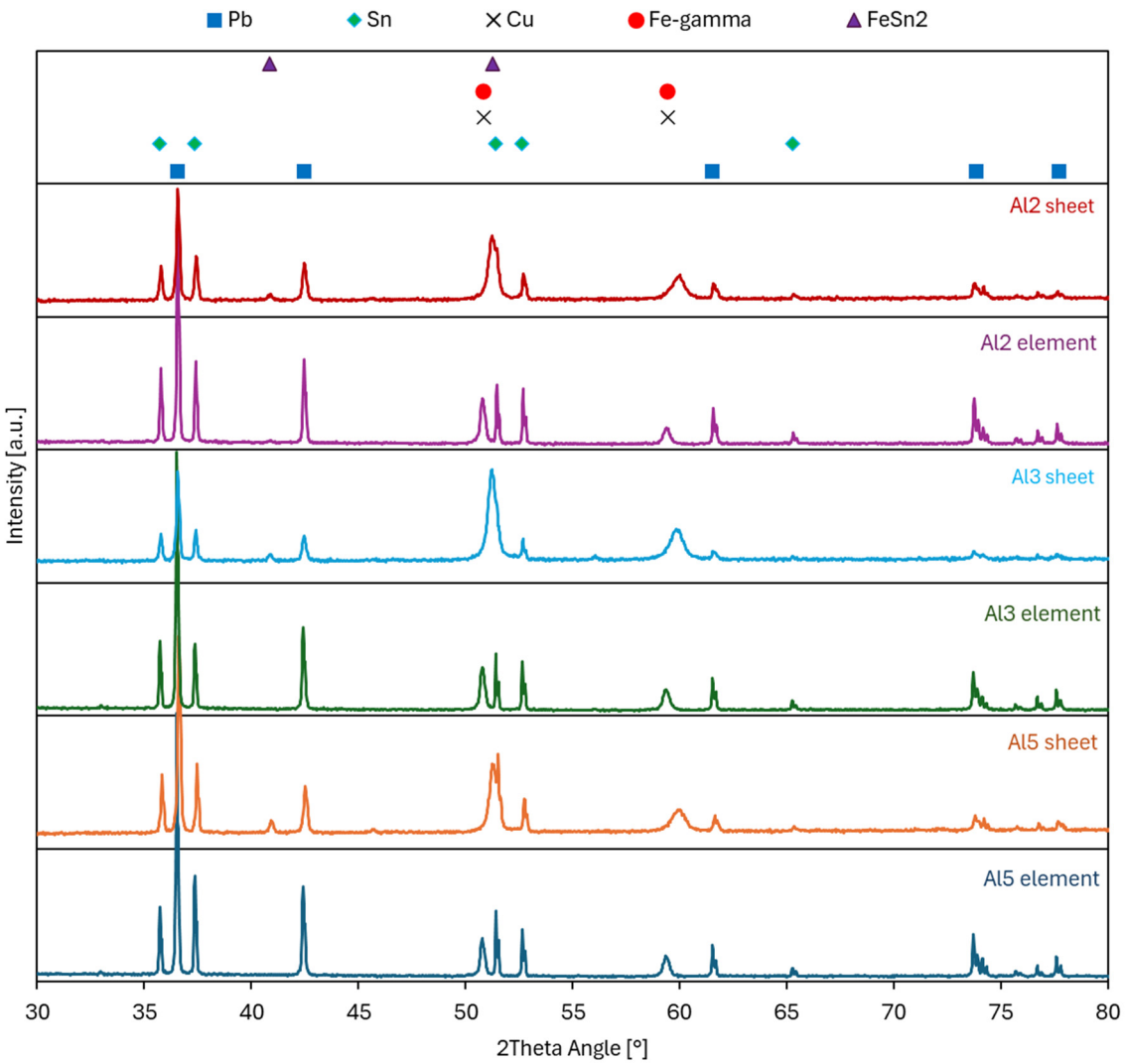


Figure 12. XRD analysis of fracture surfaces of AISI 304 steel–AW-1050A aluminum alloy RES joints (Al2, Al3, Al5).

4. Conclusions

The following conclusions were drawn from a study joining AISI 304 stainless steel to PMMA thermoplastic or AW-1050A aluminum alloy using RES technology with a bimetallic element. Sn60Pb40 solder and Chemet CHM-A-014 flux represent the right combination for preparing RES joints. The solder wets the surface of AISI 304 stainless steel very well. At a temperature of 225 °C for 5 min, the wetting angle was measured to be $\alpha = 14°$.

During soldering, solder remelting occurred in the core of the bimetallic element, alongside the rare occurrence of porosity, which was localized outside the contact area between the element and the steel sheet. The use of resistance soldering with a rapid temperature cycle made it possible to produce a soldered joint with the desired temperature gradient. At the electrode–element interface, there was solid-state contact during soldering, which is important for the lifetime of the electrode.

In the strength test of the RES joints, the measured strength ranged from 25.5 to 36.4 MPa, which reached 65 to 93% of the shear strength of the solder. All joints broke at the AISI 304 steel–Sn60Pb40 solder interface.

Observation and XRD analysis of the fracture surfaces showed that the majority of the fracture surface passed through the solder. Small areas representing the surface of AISI 304 steel were also present on the fracture surface. At these locations, the formation of the

intermetallic phase $FeSn_2$ was observed, which was formed at the AISI 304 steel–Sn60Pb40 solder interface due to the reaction of the solder with the steel surface.

The obtained results provide new knowledge about the microstructure and properties of soldered joints of the selected material combination made by resistance heating. Further research will be focused on replacing the Sn60Pb40 solder with the lead-free Sn91Zn9 solder, which has already proven itself in the production of joints of galvanized steel sheets with PMMA using RES technology.

Author Contributions: Conceptualization, methodology, investigation, writing—original draft, formal analysis, visualization P.S.; formal analysis, investigation, writing—review and editing, visualization P.Š., B.V., Z.G.; formal analysis, investigation, writing—review and editing A.S.; investigation P.G. and M.Z. All authors have read and agreed to the published version of the manuscript.

Funding: This research was funded by the Ministry of Education, Research, Development and Youth of the Slovak Republic VEGA, grant number [1/0302/23]; University Science Park of the Slovak University of Technology in Bratislava, grant number [26240220084]; Advancing University Capacity and Competence in Research, Development and Innovation, Accord 2, grant number [313021BXZ1].

Data Availability Statement: The original contributions presented in the study are included in the article. Further inquiries can be directed to the corresponding author..

Conflicts of Interest: The authors declare no conflicts of interest.

References

1. Bobovnikov, O.; Klitnoi, V.; Nepokupna, T.; Mendonça, J.P.; Ruzmetov, A. Reliability of Quartz Glass-to-Stainless Steel Connection Performed by Ultrasonic Soldering for NaI:Tl Ruggedized Detector. In *Lecture Notes in Mechanical Engineering IV, Proceedings of the International Conference Innovation in Engineering, Prague, Czech Republic, 18–20 June 2025*; Machado, J., Trojanowska, J., Ottaviano, E., Xavior, M.A., Valášek, P., Basova, Y., Eds.; Springer: Cham, Switzerland, 2025; pp. 90–100.
2. Rosario Rodriguez, G.; Beckert, E.; Hornaff, M.; Peschel, T.; Schmidt, T.; Heimberg, M. Laser beam soldering of exotic optic materials. In *SPIE 12777, Proceedings of the International Conference on Space Optics—ICSO 2022, Dubrovnik, Croatia, 3–7 October 2022*; Minoglou, K., Karafolas, N., Cugny, B., Eds.; SPIE: Dubrovnik, Croatia, 2023. [CrossRef]
3. Tayier, W.; Janasekaran, S.; Jamadon, N.H. Microstructural Analysis and Microhardness Evaluation of Stainless Steel SS304 Joints Utilizing Microwave Hybrid Heating (MHH) and Cold/Heat Processing: A Fuzzy Logic Approach. *Key Eng. Mater.* **2024**, *982*, 51–66. [CrossRef]
4. Liu, Y.; Li, G.; Wang, S.; Han, X.; Wang, B.; Ye, J. Microstructure and properties of stainless steel sheet laser soldering joint. *Trans. China Weld. Inst.* **2023**, *44*, 45–49. [CrossRef]
5. Wang, J.; Wang, S.; Wang, B.; Han, X.; Liu, Y.; Ye, J.; Cheng, Z. Study on Corrosion Resistance of Stainless-Steel Welded Joints with SnSb8Cu4 and SnZn9. *Materials* **2023**, *16*, 3908. [CrossRef]
6. Sejč, P.; Gábrišová, Z.; Vanko, B.; Schrek, A. Joining of galvanized steel sheets and aluminum by REW technology using AlSi5 joining elements. *Met. Mater.* **2019**, *57*, 287–298. [CrossRef]
7. Sejč, P.; Vanko, B.; Gábrišová, Z. REW Application Possibilities for the Production of Combined Metal—Plastic Joints. *Manuf. Technol.* **2021**, *21*, 682–690. [CrossRef]
8. Sejč, P.; Vanko, B.; Schrek, A.; Gábrišová, Z. Use of Sn60Pb40 Solder in Resistance Element Soldering Technology. *Metals* **2023**, *13*, 1313. [CrossRef]
9. Koleňák, R.; Provazník, M.; Koleňáková, M. A comprehensive investigation of copper tube joints made by resistance soldering. *Teh. Vjesn.* **2013**, *20*, 391–395.
10. Sun, Z.; Sang, J.; Sui, Y.; Wang, B.; Zang, H. Study on brass and 304 stainless steel packaging process by resistance soldering. *Trans. China Weld. Inst.* **2019**, *40*, 137–142. [CrossRef]
11. Hu, X.; Zou, G.; Dong, S.J.; Lee, M.Y.; Jung, J.P.; Zhou, Y. Effects of steel coatings on electrode life in resistance spot welding of galvannealed steel sheets. *Mater. Trans.* **2010**, *51*, 2236–2242. [CrossRef]
12. Williams, N.T.; Parker, J.D. Review of Resistance Spot Welding of Steel Sheets Part 2 Factors Influencing Electrode Life. *Int. Mater. Rev.* **2004**, *49*, 77–108. [CrossRef]
13. Sheikhi, M.; Valaee-Tale, M.; Mazaheri, Y.; Usefifar, G.R. Electrode lifetime in resistance spot welding of coated sheets: Experiments and modeling. *Mater. Today Commun.* **2024**, *38*, 107903. [CrossRef]
14. Welding Science & Technology. *Welding Handbook*, 10th ed.; American Welding Society: Miami, FL, USA, 2019; Volume 1, p. 891.

15. *Soldering Handbook*, 3rd ed.; AWS: Singapore, 1999; ISBN 0-87171-618-6.
16. Peng, Y.; Zhang, H.; Tan, T.; Fu, Z.; Guo, X. Study on ductile-to-brittle transition behavior and fracture mechanisms of Sn-based solder alloys under cryogenic impact loading. *Cryogenics* **2025**, *151*, 104173. [CrossRef]
17. He, J.; Ling, Y.; Lei, D. Mechanical properties of Sn–Pb based solder joints and fatigue life prediction of PBGA package structure. *Ceram. Int.* **2023**, *49*, 27445–27456. [CrossRef]
18. Ettefagh, A.H.; Guo, S.; Raush, J. Corrosion performance of additively manufactured stainless steel parts: A review. *Addit. Manuf.* **2021**, *37*, 101689. [CrossRef]
19. Schweitzer, P.A. *Fundamentals of Metallic Corrosion*, 2nd ed.; CRC Press: Boca Raton, FL, USA, 2007; p. 727, ISBN 10: 0-8493-8243-7.
20. Clayton, C.R.; Olefjord, I. Passivity of Austenitic Stainless Steels. In *Corrosion Mechanisms in Theory and Practice*, 2nd ed.; CRC Press: New York, NY, USA; Basel, Switzerland, 2002; pp. 217–242.
21. Olsson, C.-O.A.; Landolt, D. Passive films on stainless steels—Chemistry, structure, growth. *Electrochim. Acta* **2003**, *48*, 1093–1104. [CrossRef]
22. Hashimoto, K.; Asami, K.; Kawashima, A.; Habazaki, H.; Akiyama, E. The role of corrosion-resistant alloying elements in passivity. *Corros. Sci.* **2007**, *49*, 42–52. [CrossRef]
23. Kerber, S.J.; Tverberg, J. Stainless steel. Surface analysis. *Adv. Mater. Process.* **2000**, *158*, 33–36.
24. Welding processes. In *Welding Handbook, Part 1*, 9th ed.; American Welding Society: Miami, FL, USA, 2015; Volume 2, 680p.
25. Gharaibeh, M.A. Material and constitutive parameters of various Pb based and Pb free solders and other interconnection materials: A collective review. *Results Eng.* **2025**, *26*, 105618. [CrossRef]
26. Villars, P. *In-Sn Binary Phase Diagram 0–100 at. %Sn*; Datasheet from "PAULING FILE Multinaries Edition—2022". Available online: https://materials.springer.com/isp/phase-diagram/docs/c_0903199 (accessed on 12 October 2025).
27. Available online: https://www.dm-consultancy.com/TR/dosya/1-59/h/aisi-340-info.pdf (accessed on 15 October 2025).
28. Available online: https://www.ftpplastics.cz/_pub-app/download-file.php?hash=67b65065a8813b49c03abdd04f97d6329b5e0e026a0c555dfb53eed8e897a626b5f8758ef6cd02722e9de7cb9cf4d30ec68f2d50cbdff3a5b7747f7d13c14bc4&action=view&filename=quinn-xt-technicka-kniha-82.pdf (accessed on 13 October 2025).
29. Calado, F.; Pragana, J.; Braganca, I.; Silva, C.; Martins, P.A.F. Resistance element welding of sandwich laminates with hidden inserts. *Int. J. Adv. Manuf. Technol.* **2022**, *118*, 1565–1575. [CrossRef]
30. Wang, S.; Li, Y.; Yang, Y.; Manladan, S.M.; Luo, Z. Resistance element welding of 7075 aluminum alloy to Ti6Al4V titanium alloy. *J. Manuf. Process.* **2021**, *70*, 300–306. [CrossRef]
31. Zheng, B.; Li, Y.; Zhang, D.; Yang, Y.; Wang, S.; Manladan, S.M.; Luo, Z. Microstructure and mechanical properties of Al/Mg resistance element welded joints. *Int. J. Adv. Manuf. Technol.* **2022**, *120*, 6315–6323. [CrossRef]
32. Manladan, S.M.; Yusof, F.; Ramesh, S.; Zhang, Y.; Luo, Z.; Ling, Z. Microstructure and mechanical properties of resistance spot welded in welding-brazing mode and resistance element welded magnesium alloy/austenitic stainless steel joints. *J. Mater. Process. Technol.* **2017**, *250*, 45–54. [CrossRef]
33. Ling, Z.; Li, Y.; Luo, Z.; Ao, S.; Yin, Z.; Gu, Y.; Chen, Q. Microstructure and fatigue behavior of resistance element welded dissimilar joints of DP780 dual-phase steel to 6061-T6 aluminum alloy. *Int. J. Adv. Manuf. Technol.* **2017**, *92*, 1923–1931. [CrossRef]
34. Manladan, S.M.; Zhang, Y.; Ramesh, S.; Cai, Y.; Ao, S.; Luo, Z. Resistance element welding of magnesium alloy and austenitic stainless steel in three-sheet configurations. *J. Mater. Process. Technol.* **2019**, *274*, 116292. [CrossRef]
35. Available online: https://www.alumeco.com/media/y3thojmp/1050a-rolled-products.pdf (accessed on 13 October 2025).
36. Schrek, A.; Vanko, B.; Sejč, P. Forming of a bimetallic element for the resistance element soldering method. *J. Met. Mater.* **2020**, *74*, 8–20. [CrossRef]
37. Available online: https://www.matweb.com/search/DataSheet.aspx?MatGUID=9aebe83845c04c1db5126fada6f76f7e&ckck=1 (accessed on 13 October 2025).
38. Available online: https://www.matweb.com/search/datasheet_print.aspx?matguid=06a31d97bb734b509043d81cf131b280 (accessed on 13 October 2025).
39. Available online: https://www.lemona.lt/Files/Instrukcijos/Pdf/F007%20-%20A-014%20-%20EN%20-%20Version%200005.pdf (accessed on 13 October 2025).
40. Zhang, H.; Senkara, J. Resisitance Welding. In *Fundamentals and Applications*, 2nd ed.; CRC Press: Boca Raton, FL, USA, 2012; ISBN 978-1-4398-5371-9.
41. Karakaya, I.; Thompson, W.T. The Pb−Sn (Lead-Tin) system. *J. Phase Equilibria* **1988**, *9*, 144–152. [CrossRef]

Disclaimer/Publisher's Note: The statements, opinions and data contained in all publications are solely those of the individual author(s) and contributor(s) and not of MDPI and/or the editor(s). MDPI and/or the editor(s) disclaim responsibility for any injury to people or property resulting from any ideas, methods, instructions or products referred to in the content.